Electrodynamic properties of coplanar waveguides made from high-temperature superconducting YBa$_2$Cu$_3$O$_{7-\delta}$ electrodes on nonlinear dielectric SrTiO$_3$ substrates

A. T. Findikoglu[a)] and D. W. Reagor
Electronic and Electrochemical Materials and Devices Group, Materials Science and Technology Division,
Los Alamos National Laboratory, Los Alamos, New Mexico 87544

K. Ø. Rasmussen, A. R. Bishop, and N. Grønbech-Jensen
Condensed Matter and Statistical Physics Group, Theoretical Division, Los Alamos National Laboratory,
Los Alamos, New Mexico 87544

Q. X. Jia, Y. Fan, and C. Kwon
Superconductivity Technology Center, Materials Science and Technology Division,
Los Alamos National Laboratory, Los Alamos, New Mexico 87544

L. A. Ostrovsky
Environmental Technology Laboratory, University of Colorado, Boulder, Colorado 80303
and Institute of Geophysics and Planetary Physics, Los Alamos National Laboratory, Los Alamos,
New Mexico 87545

We present a comprehensive study of broadband (0–2 GHz) electrodynamic properties of coplanar waveguides made from high-temperature superconducting thin-film YBa$_2$Cu$_3$O$_{7-\delta}$ electrodes on nonlinear dielectric single-crystal SrTiO$_3$ substrates. The waveguides exhibit strong dielectric nonlinearities, in addition to temperature-, dc-bias-, and frequency-dependent dissipation and refractive index. By using parameters determined from small-signal (linear) transmission characteristics of the waveguides as a function of dc bias, we develop a model equation that successfully predicts and describes large-signal (nonlinear) behavior. © *1999 American Institute of Physics.* [S0021-8979(99)03615-4]

I. INTRODUCTION

With changing emphasis in high-temperature superconductor (HTS) electronics research from single-layer thin films to multilayered thin film structures, there has been renewed interest in high-frequency applications of metal-oxide-based nonlinear dielectrics (NLDs), such as SrTiO$_3$ (STO), in combination with HTS electrodes.[1–3] In essence, devices based on HTS/NLD structures promise to perform much better than their normal-metal/NLD predecessors due to: (i) reduced operational temperature leading to, in certain cases, lower dielectric loss, larger nonlinearity, and shorter relaxation times in the dielectric; (ii) lower conductor loss, and no intrinsic dispersion up to very high frequencies (~THz) in the superconducting electrodes; and (iii) "cleaner" electrode-dielectric interface leading to lower interface loss and negligible Shottky barriers. These HTS/NLD structures are attractive not only for immediate implementation in practical devices such as frequency-agile microwave filters,[4] but also for the exploration of novel scientific and technological concepts such as study of stochastic effects and pulse shaping.[5]

One of the most crucial features of this developing technology based on HTS/NLD structures is the ability to miniaturize substantially, i.e., to prepare compact devices. The importance of compact size for integration with other potential circuit components is clear. But, more importantly, since nonlinear effects in a dielectric are a function of the electric field applied to the dielectric, the smaller separation of electrodes allows for the realization of the same effects with smaller signal and control voltage levels. Whereas the dielectric loss is mostly determined by the loss tangent of the material irrespective of its size, the conductor loss, which is proportional to the surface resistance (R_s) of the electrodes, increases strongly with decreasing conductor separation. Thus, the very low R_s of superconducting electrodes [$\sim\mu\Omega$ below about 80 K at 1 GHz for YBa$_2$Cu$_3$O$_{7-\delta}$ (YBCO)] permits designs of compact devices with practically low operational voltage levels (~1–10 V).

Most potential applications would require thin films of both the NLD and the HTS material on an appropriate low-loss substrate. However, at present, even the highest quality NLD films show much smaller dielectric constant and nonlinearity, and higher dielectric losses than their single-crystal NLD counterparts.[6] Also, the functional dependence of dielectric properties on external electric field bias seems to be quite different in thin films (for example, whereas the dielectric loss decreases with bias in thin films, it increases in single crystals).[7] Currently, several approaches are being explored to make films with improved properties; such as chemical doping,[8,9] use of heteroepitaxial buffer layers,[10] and release of films from substrates by selective etching.[11] While
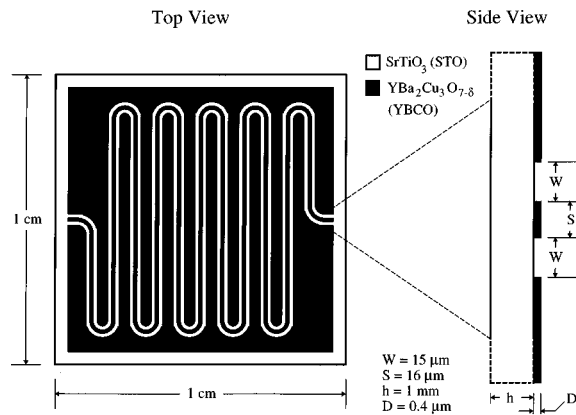
a)Electronic mail: findik@lanl.gov

FIG. 1. Schematic coplanar waveguide (CPW) device structure.

FIG. 2. Schematic measurement setup.

the effort on improving the properties of NLD films continues, it is also important to explore, in parallel, device concepts using the single crystals that possess intrinsic and more reproducible properties.

In the following, we will summarize our work on prototype nonlinear devices based on YBCO coplanar waveguide electrodes on single-crystal STO substrates. To facilitate extensive study of nonlinear and dispersive effects (which will be described later), we have adopted a time-domain measurement technique,[12] which allows for separation of dc-bias effects and high-frequency effects, and uses electrically distributed transmission line concepts for analysis. The use of distributed coplanar waveguides has enabled us to investigate the high-frequency properties of STO single crystals with high resolution because of the long interaction lengths. Among several different lengths for the coplanar waveguide, 8 cm provided the best compromise between overall dissipation and cumulative nonlinear/dispersive effects.

II. DEVICE FABRICATION

A schematic of our coplanar waveguide device structure and its pertinent dimensions are shown in Fig. 1. The electrodes are 0.4-μm-thick YBCO films, patterned in the form of 8-cm-long meandering coplanar waveguides. The YBCO films were pulsed-laser deposited (from a stoichiometric target) on 1 cm$\times$1 cm$\times$1 mm (100) single-crystal STO substrates at a substrate temperature of 780 °C in 200 mTorr O_2. The pulsed laser used is a Xe–Cl excimer laser operating at 308 nm wavelength with a repetition rate of 20 Hz and laser energy density of 2 J/cm^2 on the target. After deposition, the electrodes were defined by standard photolithography, and patterned by dilute phosphoric acid (500 ppm H_3PO_4), followed by rf sputtering of 0.5-μm-thick Au contact pads on both ends of the centerline and ground planes. As a last processing step, the devices were annealed at 400 °C for 12 h in flowing O_2.

III. MEASUREMENT SETUP

Figure 2 shows the measurement setup we used for broadband time-domain characterization of these nonlinear devices. The sample housing was designed specifically for t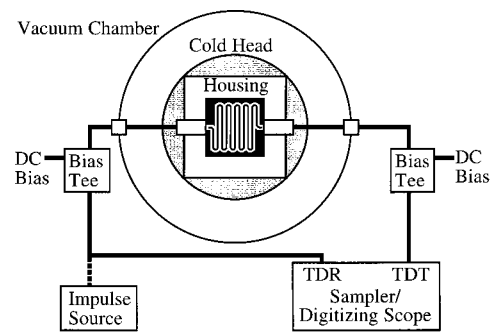his experiment: it uses a suspended-substrate geometry without sidewalls to reduce and attenuate unwanted housing modes; no external pressure is applied on the substrate to reduce complications due to possible piezoelectric effects (i.e., the substrate is unclamped); short ($\sim$2 mm) coplanar waveguide segments with 50 Ω characteristic impedance are used as an intermediate adapter to guide broadband electromagnetic waves from cylindrical symmetry of the coaxial cable to coplanar waveguide symmetry of the device; and short ($\sim$1 mm) and low-inductance ($\sim$2 nH) Au wires are used to bond the electrodes of the device to the intermediate adapter.

The housing is clamped on a cold head of a cryostat in a vacuum chamber. The input and output ports of the housing are connected with coaxial cables to the instruments outside the chamber via hermetically sealed connectors attached to ports of the chamber. The bias Tees are essentially rf chokes, which allow the dc bias to be separated from high-frequency signals. The high-frequency channel is a bandpass filter with 3 dB cutoff frequencies of 20 kHz and 12.5 GHz.

For our high-frequency device characterization, we have used two different measurement configurations; the standard step-pulse time-domain-reflection/time-domain-transmission (TDR/TDT) configuration, and the impulse-TDT configuration. The standard TDR/TDT configuration uses a 0.2 V step pulse with a 10%–90% rise time of about 30 ps as the excitation signal, and monitors the reflected (transmitted) signals from (through) the device as a function of time. The impulse-TDT configuration (connection of which is shown in a dashed line in Fig. 2) uses a Gaussian-like pulse with about 0.4 ns full width at half maximum and with varying amplitudes (between 0.2 and 40 V) as the excitation signal and monitors only the transmitted signal. The step-pulse TDR/TDT configuration has been best suited for the overall characterization of the devices in the small-signal limit and as a function of dc bias, whereas impulse-TDT configuration has been essential for the study of nonlinear/dispersive effects in the large-signal limit.

IV. ELECTRICAL CIRCUIT MODEL AND FORMALISM

In the analysis of broadband characteristics of our devices, we will use an electrical circuit model based on lumped circuit element equivalents of coupling inductance L_c and input/output impedance Z_L for the external circuitry; and distributed element equivalents of series resistance R,
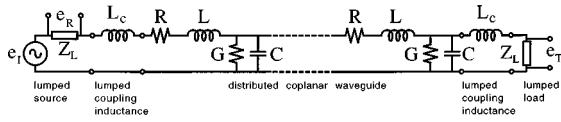
FIG. 3. Electrical circuit model.

FIG. 4. Step-pulse time-domain reflection (TDR) response. Solid lines are linear approximations.

series inductance L, shunt conductance G, and shunt capacitance C per unit length of the coplanar waveguide (see Fig. 3).

In their most general form, the inductance and impedance of the lumped elements are constants; and those of the distributed circuit elements depend on angular frequency ω, temperature T, bias voltage ν_{dc}, and signal voltage ν_s. The characteristic impedance Z_0 and propagation function γ of the coplanar waveguide are given by[13]

$$Z_0 = \sqrt{(R+i\omega L)/(G+i\omega C)} \qquad (1)$$

and

$$\gamma = \sqrt{(R+i\omega L)(G+i\omega C)} = \alpha + i\frac{\omega}{c}n, \qquad (2)$$

where c is the speed of light in vacuum, α is the attenuation constant, and n is the effective refractive index. Assuming R and G are, respectively, much smaller than ωL and ωC (in other words, series and shunt losses are small), we obtain

$$n = c\sqrt{LC} \qquad (3)$$

and

$$\alpha = \frac{R}{2\sqrt{L/C}} + \frac{G}{2\sqrt{C/L}}. \qquad (4)$$

Physically, L and C are related to the magnetic and the electric field energy stored in the waveguide, respectively. C is solely determined by the shunt geometric capacitance of the waveguide, whereas L has contributions both from the series geometric inductance of the waveguide and the surface inductance of the electrodes. R signifies dissipative losses in the series channel and is dominated by the surface resistance of the YBCO electrodes. G combines both the dissipative losses in the dielectric medium and the radiative losses through the dielectric. As will be described later, various approximations will be necessary to calculate these parameters under specific conditions.

In TDR/TDT measurements, the shape of the reflected and transmitted pulses reveals detailed information about the waveguide.[14] Depending on the characteristic impedance mismatch between the external circuitry and the waveguide, the step-pulse TDR/TDT may show staircase-like buildup of signal due to multiple reflections at the boundaries of device and external circuitry. For times less than 2τ (i.e., for primary reflection), where τ is the time it takes for the electrical pulse front to propagate the whole length l of the waveguide, the reflection coefficient ρ in the frequency domain is given by

$$\rho(\omega) = \frac{e_R(\omega)}{e_I(\omega)} = \frac{Z_0 + i\omega L_c - Z_L}{Z_0 + i\omega L_c + Z_L}, \qquad (5)$$
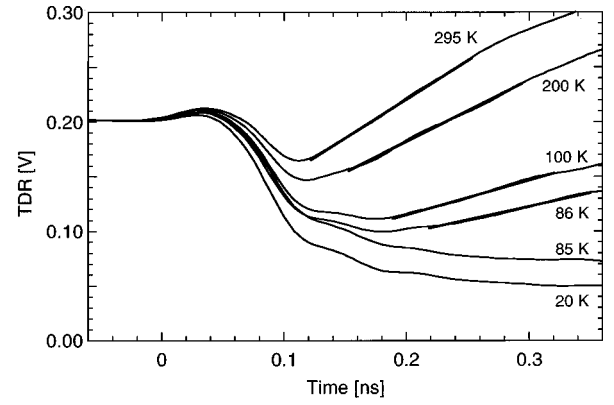
where e_I and e_R are spectral components of the incident and reflected pulse voltages, respectively. Similarly, for times less than 3τ (i.e., for primary transmission), the transmission coefficient η is given by

$$\eta(\omega) = \frac{e_T(\omega)}{e_I(\omega)} = \frac{4Z_0 Z_L}{(Z_0 + i\omega L_c + Z_L)^2}\exp[-\gamma l], \qquad (6)$$

where e_T is a spectral component of the transmitted pulse voltage. We note that the Eqs. (5) and (6) assume that the waveguide properties are uniform along the propagation direction. In the time domain, the TDR response and the TDT response are given by

$$\mathrm{TDR}(t) = e_R(t) = \mathcal{F}^{-1}\{\rho(\omega)\mathcal{F}[e_I(t)]\} \qquad (7)$$

and

$$\mathrm{TDT}(t) = e_T(t) = \mathcal{F}^{-1}\{\eta(\omega)\mathcal{F}[e_I(t)]\}, \qquad (8)$$

where $\mathcal{F}$ and $\mathcal{F}^{-1}$ denote Fourier and inverse Fourier transforms, respectively. To be specific, in our experimental arrangement, the incident pulse is actually added to the reflected pulse with a setup-specific delay. Nevertheless, in the case of step-pulse excitations, this merely adds a constant to the TDR response given in Eq. (7), and thus will be ignored for simplicity in the following analysis.

V. ELECTRICAL CHARACTERISTICS ABOVE T_c

Above the superconducting transition temperature T_c of the electrodes, the surface resistance R_s of the electrodes is expected to dominate over all other sources of loss. In fact, since YBCO films in the normal state are highly resistive (resistivity $\rho \sim 10^2$ $\mu\Omega$ cm at 100 K),[15] the transmitted power in our TDR/TDT configuration is immeasurably low. In this limit, we can learn about the device only from its TDR response. Figure 4 shows the TDR response for a 0.2 V incident step pulse at various temperatures.

The initial steep drop in amplitude is due to characteristic impedance mismatch between the 50 Ω external circuitry and the low-impedance ($\sim$2–10 Ω) waveguide. As the temperature decreases, the dielectric constant of STO increases which in turn leads to lower Z_0, and thus larger impedance mismatch and larger drop in the TDR response amplitude. At longer delay times, on the other hand, the almost linear in-

crease in the amplitude between about 0.1 and 0.3 ns is determined by both the characteristic impedance of the waveguide and the surface resistance of the electrodes. For step-pulse excitation, it is more convenient to use Laplace transform $\mathcal{L}$ (in terms of complex angular frequency s, or $i\omega$) instead of Fourier transform. Thus, using Eqs. (1), (5), and (7) in the limit G goes to zero and R is much smaller than ωL, and substituting a step pulse with an amplitude of E_I and a rise time of τ_e for e_I we obtain

$$\mathrm{TDR}(t) = \mathcal{L}^{-1}\left[\left(\frac{\sqrt{\dfrac{L}{C}} + sL_c + \dfrac{R/2}{s\sqrt{L/C}} - Z_L}{\sqrt{\dfrac{L}{C}} + sL_c + \dfrac{R/2}{s\sqrt{LC}} + Z_L}\right)\right.$$

$$\left. \times E_I\left(\frac{1}{s} - \frac{1}{s+\tau_e}\right)\right]. \qquad (9)$$

From reflection measurements without the waveguide but including effects due to the connectors, the coaxial cables, and the bias Tee, we measure τ_e to be about 40 ps. For times t much longer than τ_e, Eq. (9) simplifies considerably. Further simplification occurs if one considers relative magnitudes of inductive $[L_c/(Z_L+\sqrt{L/C})]$ and capacitive $[(Z_L+\sqrt{L/C})/(2\sqrt{LC}/R)]$ time constants of the device, and realizes that, due to very small L_c ($\sim$2 nH), the linear slope regime is dominated by the capacitive time constant of the waveguide. Thus, in these limits, the slope m of the TDR response is given by

$$m = \frac{E_I Z_L R}{\left(\sqrt{\dfrac{L}{C}} + Z_L\right)^2 \sqrt{LC}}. \qquad (10)$$

In our experimental setup, Z_L is 50 Ω. Also, we can readily calculate L and C (using conformal mapping) at any temperature, or directly measure them below T_c with standard TDR/TDT measurements (as will be further discussed in Sec. VI). The agreement is very good between calculations and measurements. In the quasistatic limit, and assuming that the thickness of the electrodes is negligibly small, L and C are given by[16]

$$L = \frac{\mu_0}{4}\frac{K(\sqrt{1-k^2})}{K(k)}, \qquad (11)$$

$$C = 4\epsilon_0 \frac{(\epsilon_r+1)}{2}\frac{K(k)}{K(\sqrt{1-k^2})}, \qquad (12)$$

where μ_0 is the permeability of vacuum, ϵ_0 is the permittivity of vacuum, ϵ_r is the relative dielectric constant of the substrate, K is the complete elliptical integral of the first kind, and the argument k is given by $S/(S+2W)$, where S is the width of the centerline and W is the width of the centerline-to-ground plane gap as shown in Fig. 1. We note
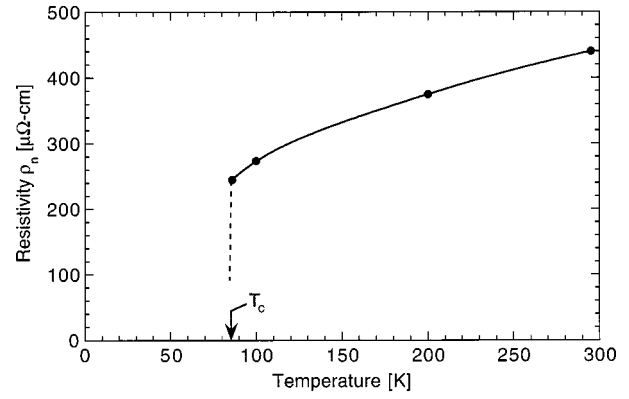

FIG. 5. Resistivity ρ_n of YBa$_2$Cu$_3$O$_{7-\delta}$ (YBCO) electrodes vs temperature.

that Eq. (11) takes into account the geometric inductance, but ignores the contribution of surface inductance of the electrodes.

Determination of conductor losses, i.e., R, is more complicated due to current crowding and skin-depth effects. In our case, the YBCO electrodes in the normal state are highly resistive and thus the skin depth is, up to very high frequencies, much larger than the film thickness. To estimate conductor loss of such a structure, we will first assume that the external field distribution will be similar to that of a film with thickness D larger than the skin depth, so that conductor loss is given by (for $D \ll S, W$)[17]

$$R = \frac{R_s}{4S(1-k^2)K^2(k)}\left[(k+1)\pi + \ln\left(\frac{4\pi S}{D}\right)\right.$$

$$\left. + k\ln\left(\frac{4\pi(S+2W)}{D}\right) - (k+1)\ln\left(\frac{1+k}{1-k}\right)\right], \qquad (13)$$

where R_s is the surface resistance of the electrodes, and then substitute thin film limit for R_s

$$R_s = \mathrm{Re}\left[\sqrt{\frac{i\mu_0\omega}{\sigma}}\coth\left(\sqrt{i\mu_0\omega\sigma}\frac{D}{2}\right)\right] \approx \frac{2}{\sigma D}, \qquad (14)$$

where σ is the normal state conductivity of the YBCO electrode and Re[ ] stands for the real part of [ ]. We note that D is scaled by 2 in Eq. (14) in order to make it compatible with Eq. (13) where magnetic fields enter from both sides of the film.[18] Since we know S, W, D, ϵ_r, and m, we can calculate $L, C,$ and R using Eqs. (10)–(13), and then solve for σ, which yields the curve shown in Fig. 5.

Considering the fact that we have made several approximations to arrive at this curve, the results are quite encouraging; the magnitude of the resistivity ρ_n and its monotonic decrease with decreasing temperature are within a factor of 2 of what we routinely measure for patterned, good quality YBCO films at dc to low frequencies.[19] Also, the fact that ρ_n does not extrapolate to zero as temperature approaches zero could be due to some extrinsic loss contribution (for example, due to a damaged resistive layer on the edges of the patterned lines of the waveguide). Nevertheless, to summarize the results in this section, we have successfully implemented the formalism described in Sec. IV to describe the behavior of our waveguides above the superconducting tran-
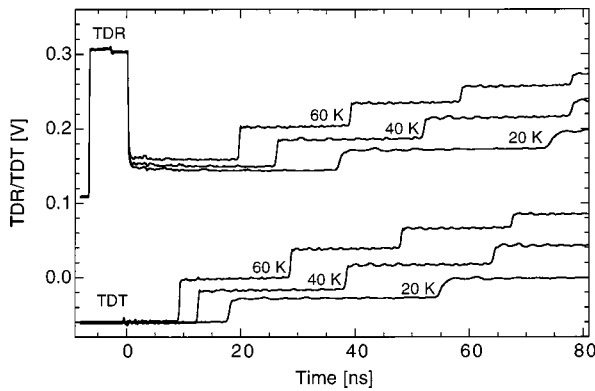
FIG. 6. Step-pulse time-domain reflection/time-domain transmission (TDR/TDT) response at different temperatures (20, 40, and 60 K).

FIG. 7. Step-pulse TDT response at 20 and 60 K at different biases (0, 5, and 10 V). The 20 K data are displaced by -0.05 V for clarity.

sition temperature T_c of its YBCO electrodes, and determined that the series resistance due to conductor losses in the electrodes is responsible for the rapid increase of TDR response for relatively short delay times (as shown in Fig. 4).

VI. SMALL-SIGNAL TDR/TDT BELOW T_c

A. Temperature and bias dependence of *C*

Once the YBCO electrodes are in the superconducting state (below about 86 K), the series resistive losses become negligibly small, and shunt losses (i.e., G) are expected to dominate dissipation in the waveguide. An appropriate expansion of Eqs. (5) and (7) in this limit shows that the TDR response for short times, as shown in Fig. 4, is insensitive to the magnitude of G for $G \lesssim 2CZ_0/L_c \sim 10^2 \, \Omega^{-1} \, \text{m}^{-1}$, which we estimate to hold in our waveguides. So, we expect the TDR response to decay exponentially with a time constant $\tau \sim L_c/(\sqrt{L/C} + Z_0)$ to the horizontal level determined by the characteristic impedance of the waveguide ($\sqrt{L/C}$), irrespective of the value of G.

One effective way to increase the resolution of our measurements is to investigate long interaction lengths (or equivalently, long interaction times). Figure 6 shows the TDR/TDT response for a 0.2 step-pulse input at various temperatures for long interaction times. The steps in the response are due to reflections from device boundaries. From the propagation difference between the steps and the step heights (and ignoring dissipative and dispersive effects for the time being), we can readily calculate L and C as a function of temperature T using Eqs. (1), (3), (5), and (6). These experimental results agree well with the predictions of our conformal mapping results [Eqs. (11) and (12)] that use, as input, waveguide dimensions and published relative dielectric constant values.[20] As a further verification, we have also measured ϵ_r of our STO substrates at low frequencies ($\sim$kHz) with an LCR meter, which yielded similar results to published data.

Figure 7 shows the TDR/TDT response at two temperatures under dc bias. The dc bias is applied between the centerline and the ground planes through a bias Tee as shown in Fig. 2. Positive voltage indicates positive bias applied to the centerline. With bias, the shunt capacitance C, and, consequently, the signal propagation speed, are reduced due to the
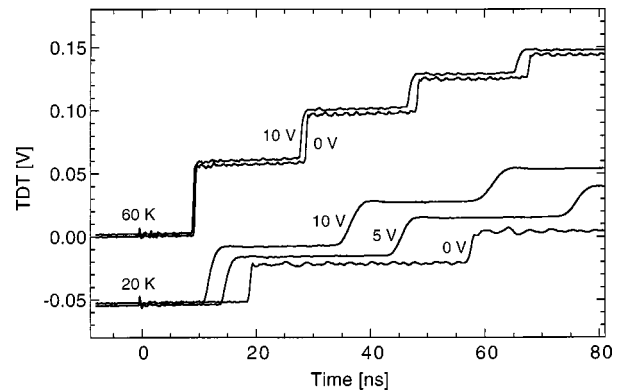
nonlinearity of ϵ_r of STO. Using an analysis similar to that used for temperature dependence, we obtain bias dependence of C, as shown in Fig. 8. As will become apparent in the following, our dc biasing scheme is a very versatile capability; it allows for an electrical control of device response characteristics, helps in distinguishing between various dispersive and nonlinear effects, and serves as a predictive tool for nonlinear response at high frequencies.

B. Dispersive and dissipative effects

A closer examination of Figs. 6 and 7 reveals that the TDR/TDT response step fronts are not as steep as the input step-pulse front (with a 10%–90% rise time of 40 ps); step fronts become broader with increasing propagation length, decreasing temperature, and increasing dc bias. This broadening could be due to dispersion and/or frequency-dependent dissipation. To quantify these dispersive and dissipative effects, one can examine spectral components of the step-pulse TDR/TDT response. Instead, we will use an equivalent method, impulse TDT analysis, to obtain the same information. We prefer impulse TDT in anticipation of the fact that, for the study of nonlinear effects described in the Sec. VII, one needs large amplitude signals, which are not as readily available in the form of short-rise time step pulses. Furthermore, Gaussian-like impulses are similar to microwave soliton solutions of many nonlinear/dispersive systems, and thus
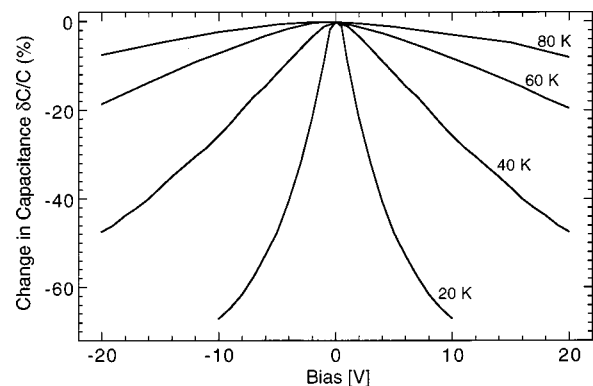

FIG. 8. Change in shunt capacitance $\delta C/C$ vs bias at different temperatures (20, 40, 60, and 80 K).
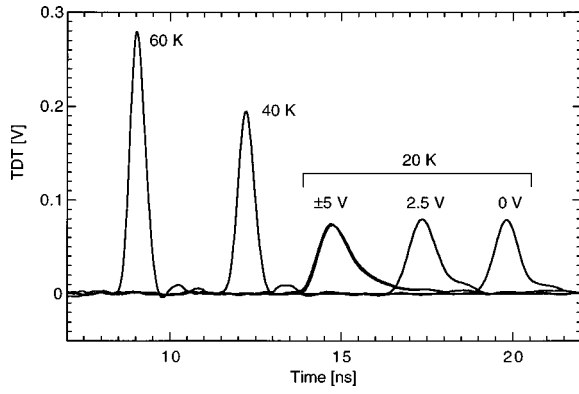
FIG. 9. Impulse TDT response at different temperatures (60, 40, and 20 K), and biases (0, +2.5, +5, and −5 V for 20 K).

FIG. 11. Refractive index $\partial \omega n(\omega)/\partial \omega$ vs frequency at different temperatures (60, 40, and 20 K) and biases (0, +5, and −5 V for 20 K). Solid lines are linear approximations.

can be used as incident pulses to investigate soliton-supporting characteristics of our waveguides.[21]

Figure 9 shows impulse TDT response at three temperatures (60, 40, and 20 K), and at three biases (+2.5, +5, and −5 V) at 20 K.

Qualitatively, the TDT response amplitude decreases (mainly due to an increase in impedance mismatch), and the delay increases (due to an increase in shunt capacitance) with decreasing temperature. To separate the intrinsic shunt losses from the impedance mismatch effect and the intrinsic dispersion from the low-pass filtering effect of the series coupling inductance, we will use slightly modified forms of Eqs. (2) and (6) to obtain spectral information about our waveguides

$$\alpha(\omega) = \frac{1}{l} \ln\left(\left|\frac{(Z_0 + i\omega L_c + Z_L)^2}{4Z_0 Z_L} \frac{e_T(\omega)}{e_I(\omega)}\right|\right) \quad (15)$$

and

$$n(\omega)\omega = \frac{c}{l} \mathrm{Arg}\left[\frac{(Z_0 + i\omega L_c + Z_L)^2}{4Z_0 Z_L} \frac{e_T(\omega)}{e_I(\omega)}\right], \quad (16)$$

where Arg[ ] stands for the argument of [ ].

Figures 10 and 11 show attenuation α and refractive index n as a function of frequency calculated using Eqs. (15)
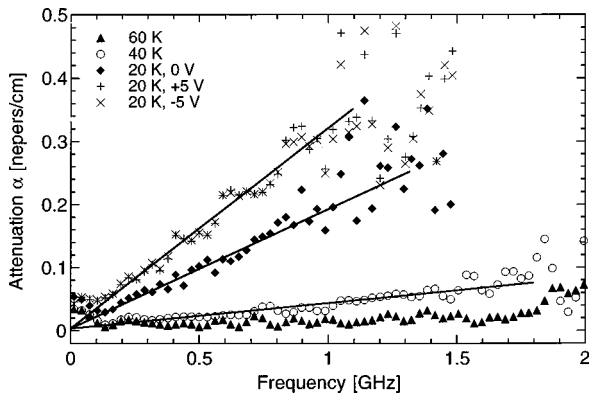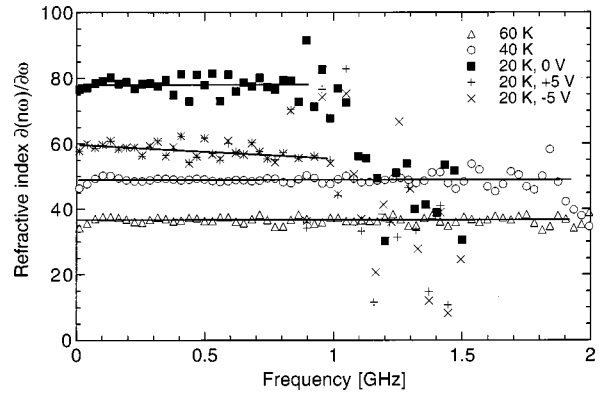

FIG. 10. Attenuation α vs frequency at different temperatures (60, 40, and 20 K) and biases (0, +5, and −5 V for 20 K). Solid lines are linear approximations.

and (16), and impulse-TDT response data shown in Fig. 9. From Eqs. (11) and (12), one can obtain, to a good approximation, ϵ_r in terms of n, given by

$$\epsilon_r = 2n^2 - 1. \quad (17)$$

Figure 11 shows, unlike Eq. (16), derivative of $\omega n(\omega)$ since changes in this quantity are easier to analyze, and the derivative reduces to n where n is frequency independent.

Between 85 and 60 K, the total attenuation is immeasurably small and the waveguide is virtually dispersionless at least up to 2 GHz. Below 60 K, the waveguide exhibits dissipation that increases approximately linearly with frequency. The dissipation increases, whereas the effective refractive index n decreases with bias. Also, we note that n becomes dispersive (high-frequency components propagate faster) at ±5 V bias. Furthermore, n at 20 K seems to have a sharp drop at around 1 GHz—the exact frequency dependence is difficult to determine due to very small signal-to-noise ratio (SNR) above 1 GHz.

The STO material is known to be quite lossy at low temperatures. In our waveguide structure, the attenuation due to the dissipation in the bulk of the dielectric (measured in terms of dielectric loss tangent tan δ) is given in the quasi-static limit by[22]

$$\alpha_d = \frac{\omega}{2c} \sqrt{\frac{\epsilon_r + 1}{2}} \left(\frac{\epsilon_r}{\epsilon_r + 1}\right) \tan \delta. \quad (18)$$

Other possible contributions to overall attenuation come from radiation and surface-wave attenuation. The radiation loss occurs because the propagating guided signal mode travels faster than the electromagnetic waves propagating in the substrate, and thus leaks energy through an electromagnetic shock wave emitted into the substrate. For our coplanar waveguide we can estimate this radiative attenuation using a quasistatic limit given by[23]

$$\alpha_{\mathrm{rad}} = \left(\frac{\pi}{8}\right)^2 \sqrt{2} \frac{\left(1 - \frac{1}{\epsilon_r}\right)^2}{\sqrt{1 + \frac{1}{\epsilon_r}}} \frac{(S + 2W)^2}{c^3 K(k) K(\sqrt{1 - k^2})} \omega^3, \quad (19)$$
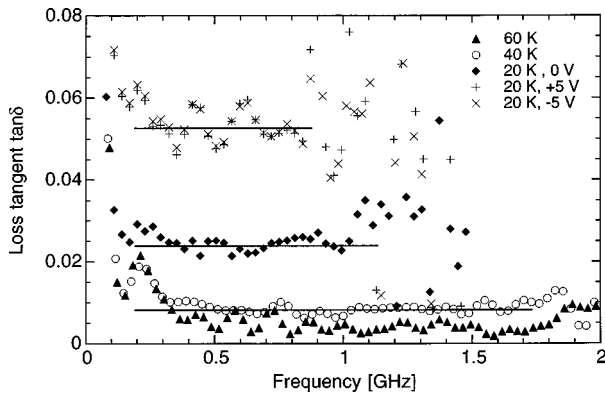
FIG. 12. Loss tangent tan δ vs frequency at different temperatures (60, 40, and 20 K) and biases (0, +5, and −5 V for 20 K). Solid lines are linear approximations.

where all quantities are as defined previously. We calculate α_{rad} to be about 4×10^{-6} Np/cm at 1 GHz at 20 K, increasing with frequency as ω^3. From this, we conclude that for the frequency range ($\leqslant 2$ GHz) in which we are interested, radiative losses are expected to be negligible.

Due to the finite thickness of the substrate and the total internal reflection from the backside of the substrate above the critical incidence angle, surface waves can be generated by the signal propagating along the waveguide.[24] In our device configuration, where the front surface of the substrate is covered with the coplanar ground planes and the backside is not metalized/grounded, we expect the lowest frequency surface-wave mode to be the TM$_0$ mode. When the propagation constant of the waveguide is almost equal to that of this surface-wave mode, the propagating signal in the waveguide is expected to exhibit a sharp increase in attenuation, and a strong dispersive behavior. The surface-wave coupling frequency f_{sw} in the vicinity of which such coupling is strong is approximated by[25]

$$f_{sw} \sim 0.3 \frac{c}{h\sqrt{\epsilon_r}}, \tag{20}$$

where h is the thickness of the substrate. By using the measured values for ϵ_r, 10 240 at 20 K and 4960 at 40 K, we obtain f_{sw} values of 0.9 and 1.3 GHz, respectively. These estimated values indicate that the strong dispersion we observe, especially around 1 GHz at 20 K, could be due to coupling of the propagating signal to the TM$_0$ surface-wave mode of the substrate.

Thus, we will make the assumption that the dielectric loss in STO dominates shunt losses in our waveguide structure in the whole range of the data shown in Fig. 10, except possibly above about 1 GHz at 20 and 40 K. Using the data shown in Fig. 10 and Eq. (18), we determine effective loss tangent tan δ as shown in Fig. 12. The seemingly high dielectric loss below about 0.2 GHz could be an artifact due to the finite time window we have used in our Fourier analysis, and the large scatter of data above 1 GHz at 20 K is due to small SNR ratio. Other than these features, we notice regions of frequency, marked by solid lines, where tan δ is frequency

independent. At 60 K, tan δ is on the order of 10^{-3}, close to our resolution limit; tan δ increases with decreasing temperature and increasing bias.

Several, but not all, features of the functional dependence of the refractive index n and the loss tangent tan δ on frequency, temperature, and bias as shown in Figs. 8, 11, and 12 are consistent with earlier experiments, and phenomenological models on STO. The STO material is known to be an incipient ferroelectric (i.e., shows paraelectric behavior at temperatures down to absolute zero),[26] and is believed to enter a quantum paralectric phase below about 4 K.[27] At large enough temperatures (above about 40 K), the increase of ϵ_r with decreasing temperature is well described by a phenomenological Curie–Weiss law with a Curie temperature of about 30 K.[28] Additionally, a generalized Lyddane–Sachs–Teller relationship based on the displacements of Ti and Sr ions and the related electrically active phonon modes satisfactorily describe the bias dependence of ϵ_r; with bias, the transverse optic mode of the lowest frequency, also called the soft phonon mode, hardens, leading to lower ϵ_r.[20] But, this model also predicts, and some other experiments support, that the soft phonon mode frequency is very high: it varies between about 2 THz at room temperature and about 0.2 THz at 4 K.[29] In our experiments (even under bias and at 20 K), these models would predict ϵ_r to remain in the quasistatic limit with no intrinsic dispersion up to about a few hundred GHz. Recent detailed calculations using similar phenomenological models also show how defects and anisotropy can influence the dielectric response; a high concentration of defects reduces nonlinearity and increases dissipation.[30,31] Comparing the bias and temperature dependence of the refractive index n shown in Fig. 11 with published data,[20,32,33] and with the predictions of phenomenological models, we deduce that our single-crystal STO substrates are of fairly good quality. Thus, the bias-dependent dispersion we have observed is unlikely to be due to extrinsic effects such as a high concentration of impurities.

At low temperatures (below about 40 K), the dielectric response in STO deviates from simple Curie–Weiss-law behavior due to collective quantum tunneling effects. In this regime, the field dependence of the dielectric constant can be modeled by a transverse-field Ising Hamiltonian that combines tunneling and external field terms.[34] This model gives support for the existence of polar clusters with a distribution of relaxation times.[35]

No comprehensive model exists for dielectric losses in STO. Some possible mechanisms for microwave dielectric losses have recently been considered by Vendik, Ter-Martirosyan, Zubko.[36] These loss mechanisms include the fundamental loss connected with multiphonon scattering of the soft phonon mode, and the transformation of electromagnetic oscillations into acoustic oscillations due to residual ferroelectric polarization or charged defects. The fundamental loss mechanism predicts increasing loss with decreasing temperature below about 60 K and with increasing bias, similar to what we observe in our experiments. However, all three mechanisms also predict linear increase of loss tangent tan δ with frequency up to 100 GHz, in contrast to the

frequency-independent behavior we have observed.

The Vendik model relies on the dielectric response of a system with a single degree of freedom.[36] However, this Debye-type[37] description is inadequate to describe the response of a system with a distribution of relaxation times, i.e., with many degrees of freedom.[38] A general empirical modification of the Debye expression which accommodates a distribution of relaxation times leads to, under certain conditions, a frequency-independent loss tangent behavior in agreement with experiments on many strongly interacting dielectric systems (i.e., systems with strong interactions among spin, charge, or lattice degrees of freedom).[39] Our observation here of a frequency-independent loss tangent implies that STO crystals need a more general treatment than that based on a weakly interacting system.

In our coplanar waveguide geometry, it is also possible that the bias dependence of attenuation and ϵ_r we have observed are not entirely intrinsic to the STO material, but are rather influenced by what might be termed ''geometric'' effects. These effects originate from the nonuniform distribution of biasing field in the nonlinear substrate (due to coplanar arrangement of the electrodes). However, since our waveguide has a lateral size of $(S+2W)\sim 50\,\mu$m, which is 20 times smaller than the smallest guided or radiated wavelength of about 1 mm (for the highest experimental frequency of interest of 2 GHz at the lowest temperature of 20 K considered), it seems plausible that an effective medium model can accurately describe its electrodynamic response. Nevertheless, for the accurate determination of geometric effects, a detailed numerical electromagnetic analysis would be necessary.

VII. LARGE-SIGNAL IMPULSE TDT

A. Biasing to control and study nonlinear effects

As we have shown in the previous sections, by applying a dc bias v_{dc}, we can change the small-signal electrical characteristics of our waveguides through changes in the shunt capacitance C and the shunt conductance G. Since the lowest electrically active transverse optic mode (or, soft phonon mode) in STO is expected to be of the order of a few hundred GHz, the dc bias effects should, ideally, provide all the information necessary for the determination of the large-signal behavior of the waveguide in the microwave frequency range up to the soft phonon mode frequency. In practice, however, such a relationship is complicated because our waveguide devices exhibit bias-dependent dispersive (i.e., bias- and frequency-dependent ϵ_r) and bias- and frequency-dependent dissipative effects at much lower frequencies—in the frequency range of our interest between 0 and 2 GHz. Since the nonlinearity, the dispersion, and the frequency-dependent dissipation all cause pulse-shaping effects of some sort (in fact, it is the balance between dispersive and nonlinear effects that could give rise to stable pulse shapes, called solitons),[40] it is necessary to distinguish among these effects for an accurate analysis of the large-signal behavior.

Figure 13 shows how one can use bias dependence to distinguish between small-signal and large-signal regimes in addition to changing the electrical characteristics of the de-
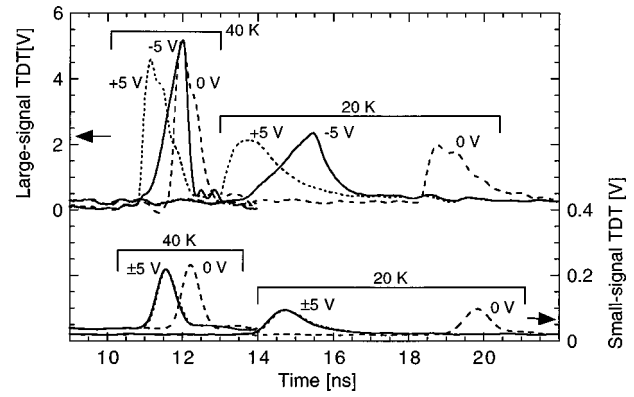

FIG. 13. Large-signal and small-signal impulse TDT response at different temperatures (40 and 20 K) and biases (0, +5, and −5 V).

vice. The bottom traces show the impulse-TDT response of the waveguide in the small-signal (linear) limit. The transmitted pulses for zero bias at both 20 and 40 K (dashed lines) have symmetric pulse shapes, similar to that of the input pulse. The transmitted pulse at 20 K has a lower amplitude mainly because of the larger impedance mismatch between the device and the external circuity [as given by Eq. (6)], and is broader because of the larger dissipation of high frequency signals at that temperature (see Fig. 10). Both +5 V (continuous line) and −5 V (dotted line) biases lead to very similar delay and pulse shapes because the pulse itself is in the small-signal limit and the bias dependence of C and G is symmetric around zero bias. With bias, the pulses become broader mainly because of the increased dissipation at higher frequencies (see Fig. 10). At 20 K and under bias, the pulse front also steepens slightly compared to the backside of the pulse because of the dispersion where high-frequency segments of the pulse experience slightly reduced index of refraction n (see Fig. 11). These linear effects have already been addressed using Fourier analysis in the previous sections.

The top traces in Fig. 13 show the combined effect of nonlinearity, dissipation, and dispersion for transmitted pulses at 20 and 40 K in the large-signal regime. For zero bias, the leading edges of the pulses exhibit shock-like steepening at both 40 and 20 K. The transmitted pulse at 20 K is of lower amplitude and broader than that at 40 K due to a combination of effects consisting of a larger impedance mismatch with external circuitry, a larger dispersion, and a larger dissipation of high-frequency signals at the former temperature. In this large-signal regime, the positive and negative biases lead to significantly different pulse shapes, the pulse at the lower temperature (20 K) showing larger change in delay due to larger nonlinearity at that temperature. The large-signal behavior can be qualitatively understood by considering the superposition of the dc bias amplitude and the amplitude of different segments of the pulse to determine the ''effective'' bias which different segments of the pulse experience. In the case of positive bias, both the bias and the pulse add constructively; thus, larger amplitude segments of the pulse experience smaller ϵ_r, and larger dispersion and dissipation compared to zero bias (see Figs. 9 and 10). As a result, the pulse tip is shifted to lower delay,
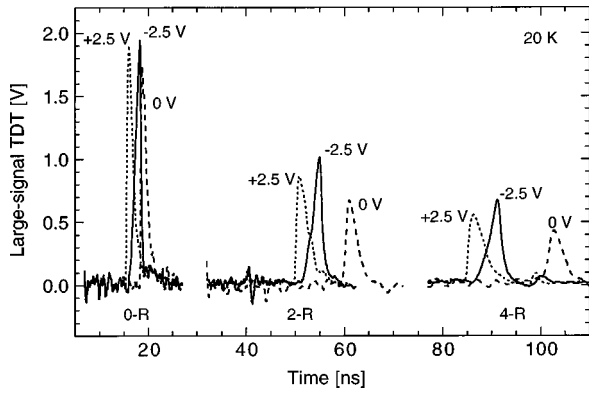
FIG. 14. Large-signal impulse TDT response at 20 K for different biases (0, +2.5, and −2.5 V) with zero, two, and four reflections (0-R,2-R,4-R) at device boundaries, with corresponding propagation lengths of l, $3l$, and $5l$, respectively.

and is rounded, and the oscillatory features in the trailing edge are more dispersed and dissipated. In the case of negative bias, pulse and bias have opposite polarities, and the pulse amplitude in the device is less than the bias amplitude in the case of −5 V bias; the peak segment of the pulse feels the smallest effective bias, thus, propagates the slowest, and experiences the lowest dispersion and dissipation among all the segments of the pulse, resulting in a pulse shape where the peak segment lags behind the pulse front and remains sharper than the lower amplitude segments.

Figure 14 shows impulse TDT response for multiple transmissions with corresponding propagation distances of l, $3l$, and $5l$, where l is the length of the waveguide. Since both the characteristic impedance mismatch between the waveguide and the external circuitry and the dissipation are quite large at 20 K, we expect the pulse within the waveguide to bounce back and forth between the device boundaries with only about 15% of the energy of the pulse being transmitted at either device boundary, but between about 50% and 90% of the overall energy being dissipated each time the pulse propagates a distance l. So, as a first approximation and ignoring frequency-dependent effects at the device boundaries, one may consider the transmitted pulses shown in Fig. 14 as sampling of the propagating pulse in an indefinitely long and uniform waveguide at different times. We see that, although the pulses get smaller and broader with time in all bias conditions, in the case of −2.5 V bias, the ''triangular'' shape of the pulse seems to be preserved. In other words, the pulse is shaped strongly by the waveguide when its amplitude is high, and this shape is somewhat preserved as the pulse makes a transition with time from large-signal to small-signal regime while the frequency-dependent dissipation acts on it.

The formalism we developed and used in the previous sections, which essentially assumes linear response, is not valid in the nonlinear regime. In the following, we will develop a new formalism for quantitative analysis of the large-signal behavior.

B. Quantitative analysis of the large-signal behavior

We have previously developed a model in the form of a nonlinear wave equation describing the signal transmission in the large-signal regime.[21] This model was based on the small-signal measurements of delay time and pulse broadening. Using these measurements to determine the nonlinearity and dispersion, we found that the validity of this model could be extended into the large-signal regime. The model was able to reproduce the basic pulse-shaping features experimentally observed. Its main flaw was that the dispersion effects seemed to be somewhat overestimated. Pursuing the philosophy that the small-signal results can be utilized to construct a model that also is valid in the large-signal regime, we will here use the improved measurements presented earlier in this article to construct a correspondingly improved model of the nonlinear pulse shaping.

There will be three components of this model; first there is the nonlinearity which is shown in Fig. 8 in the form of a bias-dependent shunt capacitance C. This results in a nonlinear velocity $u(\nu) = 1/\sqrt{C(\nu)L}$, where L is the linear series inductance, and ν is the sum of dc-bias voltage ν_{dc} and signal voltage ν_s, as defined earlier. Second, Fig. 10 shows that the attenuation is strongly frequency dependent—this is a new observation which was not available at the time of the previous work,[21] and will become an important factor in the improved model we develop here. As seen from Fig. 10, the attenuation α depends basically linearly on the frequency as $\alpha = \alpha_0 \omega$ where α_0 is to be extracted from the measurements and will clearly depend on the bias voltage and the temperature. Finally, Fig. 11 suggests that dispersion also plays a role at least for nonzero bias. Figure 11 shows that the frequency dependence of the refractive index is of the form $n = n_0 - n_1 \omega$ which yields a contribution of the form $\omega/k = u_0(\nu_{dc}) + u_1(\nu_{dc})k$ to the dispersion relation. The next step is then to write down a model equation that reproduces these three characteristics in the linear (small-signal) limit. This is achieved by

$$\frac{\partial \nu_s}{\partial t} + u(\nu_{dc} + \nu_s) \frac{\partial \nu_s}{\partial x} = \left(\alpha \frac{\partial}{\partial x} + \beta \frac{\partial^2}{\partial x^2} \right) H\{\nu_s\}, \quad (21)$$

where

$$H\{\nu_s\} = \frac{1}{\pi} \int_{-\infty}^{\infty} \frac{\nu_s(\xi)}{\xi - x} d\xi \quad (22)$$

is the Hilbert transform. In contrast to our earlier model,[21] we have here limited the model to describe propagation in one direction. This has been done for convenience and does not limit the generality of the model.

In the linear limit Eq. (21) has the dispersion relation

$$\omega = u(\nu_{dc})k - i\alpha|k| + \beta k|k|, \quad (23)$$

which contains the components described above. The parameters α and β are to be determined from Figs. 10 and 11, respectively. The coefficients α and β will depend parametrically on the bias voltage and the temperature.

In the limit of weak nonlinearity, $\nu_{dc} < 0$, and without losses, Eq. (21) reduces to the Benjamin–Ono[41–43] equation describing internal wave propagation in stratified fluids.
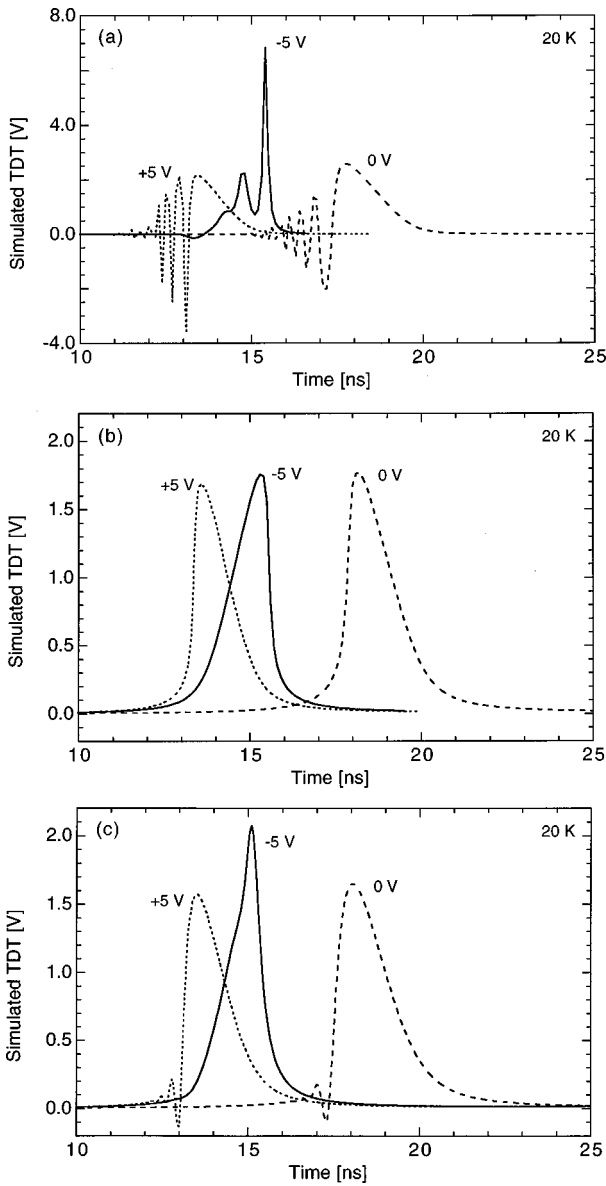
FIG. 15. Simulated large-signal impulse TDT response at 20 K for different biases (0, +2.5, and −2.5 V) with (a) $\alpha=0$, $\beta=\beta_{exp}$ (lossless), (b) $\alpha=\alpha_{exp}$, $\beta=0$ (dispersionless), and (c) $\alpha=\alpha_{exp}$, $\beta=\beta_{exp}$.

FIG. 16. Simulated large-signal impulse TDT response at 20 K for different biases (0, +2.5, and −2.5 V) with zero, two, and four reflections (0-R,2-R,4-R) at device boundaries, with corresponding propagation lengths of l, $3l$, and $5l$, respectively.

Equation (21) has been derived in a phenomenological way and therefore the microscopic physical origins of the dispersion and attenuation terms in it are not clear at this point.

As a test of the model we numerically simulate the pulse propagation for $T=20$ K for the cases $\nu_{dc}=0$, -5 V, $+5$ V, and compare these results with those of the experiments shown in Fig. 13. To illustrate the relative influence of dispersion and frequency-dependent attenuation, we show in Fig. 15 three cases; (a) $\alpha=0$, $\beta=\beta_{exp}$ (lossless), (b) $\alpha=\alpha_{exp}$, $\beta=0$ (dispersionless), and (c) $\alpha=\alpha_{exp}$, $\beta=\beta_{exp}$. Here the subscript exp denotes that the values have been determined from Figs. 10 and 11. The lossless case (a) has similar features to the model proposed in Ref. 21 in the sense that the main pulse-shaping features of the experiment are reproduced. It also suffers from the same flaw; namely, strong oscillations in the pulse front. In the dispersionless case (b) the pulse-shaping features of the experiment are
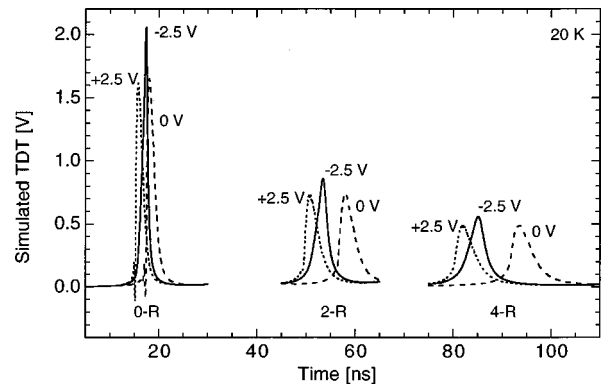
present. However, the pulses under bias show almost mirror symmetry in their shape and are rather smooth as a result of the attenuation. Particularly, the pulse for negative bias has lost the sharp peak that the experiments show. Finally, the case where both dispersion and attenuation are present (c) reproduces the experimental features very well, and the oscillations at the front are minor. It is therefore apparent that our model with appropriate choice of parameter values for α and β successfully predicts the large-signal behavior of our waveguides, and we can conclude that all of the three components of nonlinearity, dispersion, and frequency-dependent attenuation are essential for the modeling.

In Fig. 16, we show examples of pulses having propagated one, three, and five device lengths l. In the experiments, the pulse experiences frequency- and amplitude-dependent reflection and transmission at the boundaries, but we are neglecting this effect in the simulations. As seen, the model reproduces the overall features of the experimental data quite well even at rather large propagation distances. Similar to the experimental results shown in Fig. 15, the simulations show that the triangular pulse shape for -2.5 V bias is somewhat preserved as the pulse propagates, while the amplitude decreases and the width increases as a result of the dissipation. Since the dissipation plays a central role in Eq. (21), pure soliton solutions are not present, though Eq. (21), in the absence of attenuation (i.e., $\alpha=0$), probably supports soliton solutions due to its close relation to the Benjamin–Ono equation which is known to be exactly integrable. To some extent, Fig. 15(a) provides evidence that Eq. (21) (with $\alpha=0$) possesses a soliton-like solution because, for $\nu_{dc}=-5$ V, the pulse begins to split in two. Such behavior is characteristic of soliton bearing equations.[44] Such soliton solutions of Eq. (21) would be interesting from a theoretical point of view since they will have algebraically decaying tails in contrast to more standard solitons with exponentially decaying tails—this will strongly influence their splitting and interaction properties.[45]

VIII. CONCLUSION

As presented above, at low temperatures our HTS/NLD prototype devices exhibit strong dielectric nonlinearities and

negligible series resistive losses from dc up to at least a few GHz, rendering them interesting for many applications at radio and microwave frequencies. Such potential applications fall into two broad categories: quasistatic and dynamic. Devices in the quasistatic category use the dielectric nonlinearity as a means of controlling the small-signal (linear) response of the device. A good example for this category is an electrically tunable multipole bandpass filter where dc or low-frequency control signals are used both to fine tune the filter profile and to broadband tune the passband for high-frequency signals.[4] In the dynamic category, devices are in the large-signal (nonlinear) regime, and thus can be used for harmonic generation and mixing,[46] parametric amplification,[47] and pulse shaping,[48] etc. In this case, dc or low-frequency signals are used to control the nonlinear response. To have a realistic assessment of the potential of HTS/NLD materials in such broad ranges of applications, it is necessary to perform a broadband electrodynamic characterization in terms of not only nonlinear effects but also dispersive and dissipative effects.

The time-domain measurement and analysis technique we have developed in this study has allowed us to carry out such a comprehensive characterization. The 8-cm-long coplanar waveguides made from YBCO electrodes on single-crystal STO substrates have exhibited dielectric nonlinearity ($\delta\epsilon_r / \epsilon_r V$) of about 1%/V at 60 K and more than 10%/V at 20 K. This nonlinearity was sustained at least up to 2 GHz at 60 K, and 1 GHz at 20 K, with corresponding frequency-independent effective $\tan \delta$ values of less than 10^{-3}, and about 2×10^{-2}, respectively. The waveguides, which were essentially dispersionless under zero bias, became dispersive under bias. With bias, the $\tan \delta$ has also increased. At present, whether all these effects are caused by purely intrinsic properties of the STO material is unclear.

Finally, by using parameters determined from small-signal (linear) transmission characteristics of the waveguides as a function of dc bias, we have constructed a phenomenological nonlinear model equation. This equation—combining nonlinearity with bias- and frequency-dependent dissipation, and bias-dependent dispersion—has accurately predicted the large-signal (nonlinear) behavior such as pulse-shaping effects, which we have experimentally observed.

[1] O. G. Vendik, L. T. Ter-Martirosyan, A. I. Dedyk, S. F. Karmanenko, and R. A. Chakalov, Ferroelectrics **144**, 33 (1993).

[2] A. T. Findikoglu, Q. X. Jia, X. D. Wu, and D. W. Reagor, Integr. Ferroelectr. **15**, 163 (1997).

[3] M. J. Lancaster, J. Powell, and A. Porch, Supercond. Sci. Technol. **11**, 1323 (1998).

[4] A. T. Findikoglu, Q. X. Jia, X. D. Wu, G. J. Chen, T. Venkatesan, and D. W. Reagor, Appl. Phys. Lett. **68**, 1651 (1996).

[5] A. T. Findikoglu, Q. X. Jia, D. W. Reagor, Y. Fan, G. D. Lythe, R. A. Camassa, D. Cai, N. Grønbech-Jensen, and A. R. Bishop, Integr. Ferroelectr. **22**, 779 (1998).

[6] O. G. Vendik, Ferroelectrics **12**, 85 (1976).

[7] S. Gevorgian, E. Carlsson, E. Wikborg, and E. Kollberg, Integr. Ferroelectr. **22**, 765 (1998).

[8] C. M. Jackson, J. H. Kobayashi, A. Lee, C. Prentice-Hall, J. F. Burch, and R. Hu, Microwave Opt. Technol. Lett. **5**, 722 (1992).

[9] S. B. Herner, F. A. Selmi, V. V. Varadan, and V. K. Varadan, Mater. Lett. **12**, 424 (1993).

[10] Q. X. Jia, A. T. Findikoglu, D. Reagor, and P. Lu, Appl. Phys. Lett. **73**, 897 (1998).

[11] M. J. Dalberth, J. C. Price, and C. T. Rogers, Mater. Res. Soc. Symp. Proc. **493**, 371 (1998).

[12] See, for example, M. J. C. van Gemert, Philips Res. Rep. **28**, 530 (1973).

[13] R. L. Kautz, J. Appl. Phys. **49**, 308 (1977).

[14] Advanced TDR Techniques, Hewlett-Packard Application Note No. 62-3, May 1990.

[15] J. M. Phillips, J. Appl. Phys. **79**, 1829 (1996).

[16] K. E. Collin, *Foundations for Microwave Engineering* (McGraw–Hill, New York, 1992), pp. 175, 176.

[17] K. E. Collin, in Ref. 16, pp. 178, 179.

[18] E. Tuncer, B. T. Lee, M. S. Islam, and D. P. Neikirk, IEEE Trans. Microwave Theory Tech. **42**, 1807 (1994).

[19] N. Newman and W. G. Lyons, J. Supercond. **6**, 119 (1993).

[20] R. C. Neville, B. Heneisen, and C. A. Mead, J. Appl. Phys. **43**, 2124 (1972).

[21] A. T. Findikoglu, D. W. Reagor, K. Ø. Rasmussen, A. R. Bishop, N. Grønbech-Jensen, Q. X. Jia, Y. Fan, and C. Kwon, Appl. Phys. Lett. **74**, 1770 (1999).

[22] S. Ramo, J. R. Whinnery, and T. Van Duzer, *Fields and Waves in Communication Electronics*, 3rd ed. (Wiley, New York, 1993), pp. 414–416.

[23] M. Y. Frankel, S. Gupta, J. A. Valdmanis, and G. A. Mourou, IEEE Trans. Microwave Theory Tech. **39**, 910 (1991).

[24] D. B. Rutledge, D. P. Neikirk, and D. P. Kasilingham, *Millimeter Components and Techniques, Infrared and Millimeter Waves, Part II*, edited by K. J. Button (Academic, New York, 1983), Chap. 1.

[25] M. Riaziat, R. Majidi-Ahy, and I. J. Feng, IEEE Trans. Microwave Theory Tech. **38**, 245 (1990).

[26] J. H. Barrett, Phys. Rev. **86**, 118 (1952).

[27] K. A. Muller and H. Burkard, Phys. Rev. B **19**, 3593 (1979).

[28] H. E. Weaver, Phys. Chem. Solids **11**, 274 (1959).

[29] R. A. Cowley, Phys. Rev. **134**, A981 (1964).

[30] O. G. Vendik and S. P. Zubko, J. Appl. Phys. **82**, 4475 (1998).

[31] O. G. Vendik and S. P. Zubko, Zh. Tekh. Fiz. **67**, 29 (1997).

[32] J. Krupka, R. G. Geyer, M. Kuhn, and J. H. Hinken, IEEE Trans. Microwave Theory Tech. **42**, 1886 (1994).

[33] K. Araki, I. Iwasa, Y. Kobayashi, S. Nagata, and M. Morisue, IEEE Trans. Magn. **25**, 980 (1989).

[34] J. Hemberger, M. Nicklas, R. Viana, P. Lunkenheimer, A. Loidl, and R. Bohmer, J. Phys.: Condens. Matter **8**, 4673 (1996).

[35] E. Courtens, B. Hehlen, G. Coddens, and B. Hennion, Physica B **220**, 577 (1996).

[36] O. G. Vendik, L. T. Ter-Martirosyan, and S. P. Zubko, J. Appl. Phys. **84**, 993 (1998).

[37] P. Debye, *Polar Molecules* (Chemical Catalog, New York, 1929).

[38] R. M. Hill and A. K. Jonscher, Contemp. Phys. **24**, 75 (1983).

[39] See, for example, M. Remoissenet, *Waves Called Solitons* (Springer, Berlin, 1994).

[40] S. Havriliak and S. Negami, J. Polym. Sci., Part C: Polym. Symp. **14**, 99 (1966).

[41] T. B. Benjamin, J. Fluid Mech. **29**, 559 (1967).

[42] H. Ono, J. Phys. Soc. Jpn. **39**, 1082 (1975).

[43] R. E. Davis and A. Acivvos, J. Fluid Mech. **29**, 593 (1967).

[44] D. Cai, N. Grønbech-Jensen, A. R. Bishop, A. T. Findikoglu, and D. Reagor, Physica D **123**, 291 (1998).

[45] Y. Matsuno, Int. J. Mod. Phys. B **9**, 1985 (1995).

[46] A. T. Findikoglu, Q. X. Jia, D. W. Reagor, and X. D. Wu, Electron. Lett. **31**, 1814 (1995).

[47] P. K. Tien, J. Appl. Phys. **29**, 1347 (1958).

[48] S. R. Wilson, M. M. Turner, and P. W. Smith, IEEE Trans. Electron Devices **38**, 767 (1991).